

Oriental tuning of the Fermi sea of confined electrons at the SrTiO₃ (110) and (111) surfaces

T. C. Rödel,^{1,2} C. Bareille,¹ F. Fortuna,¹ C. Baumier,¹ F. Bertran,² P. Le Fèvre,² M. Gabay,³ O. Hijano Cubelos,³ M. J. Rozenberg,^{3,4} T. Maroutian,⁵ P. Lecoeur,⁵ and A. F. Santander-Syro^{1,*}

¹*CSNSM, Université Paris-Sud and CNRS/IN2P3, Bâtiments 104 et 108, 91405 Orsay cedex, France*

²*Synchrotron SOLEIL, L'Orme des Merisiers, Saint-Aubin-BP48, 91192 Gif-sur-Yvette, France*

³*Laboratoire de Physique des Solides, Université Paris-Sud and CNRS, Bâtiment 510, 91405 Orsay, France*

⁴*Depto. de Física - IFIBA Conicet, FCEN, UBA,*

Ciudad Universitaria P.1, 1428, Buenos Aires, Argentina

⁵*Institut d'Electronique Fondamentale, Université Paris-Sud and CNRS, Bâtiment 220, 91405 Orsay, France*

We report the existence of confined electronic states at the (110) and (111) surfaces of SrTiO₃. Using angle-resolved photoemission spectroscopy, we find that the corresponding Fermi surfaces, subband masses, and orbital ordering are different from the ones at the (001) surface of SrTiO₃. This occurs because the crystallographic symmetries of the surface and sub-surface planes, and the electron effective masses along the confinement direction, influence the symmetry of the electronic structure and the orbital ordering of the t_{2g} manifold. Remarkably, our analysis of the data also reveals that the carrier concentration and thickness are similar for all three surface orientations, despite their different polarities. The orientational tuning of the microscopic properties of two-dimensional electron states at the surface of SrTiO₃ echoes the tailoring of macroscopic (*e.g.* transport) properties reported recently in LaAlO₃/SrTiO₃ (110) and (111) interfaces, and is promising for searching new types of 2D electronic states in correlated-electron oxides.

Two-dimensional electron gases (2DEGs) in transition-metal oxides (TMOs) present remarkable phenomena that make them unique from a fundamental viewpoint and promising for applications [1, 2]. For instance, heterostructures grown on the (001) surface of SrTiO₃, a TMO insulator with a large band-gap of ~ 3.5 eV, can develop 2DEGs showing metal-to-insulator transitions [3], superconductivity [4], or magnetism [5, 6]. Recently, 2DEGs at the (111) and (110) interfaces of LaAlO₃/SrTiO₃ were also reported [7]. The latter showed a highly anisotropic conductivity [8] and a superconducting state spatially more extended than the one at the (001) interface [9]. Interestingly, theoretical works have also predicted that exotic, possibly topological, electronic states might occur at interfaces composed of (111) bilayers of cubic TMOs [10–13], as two (111) planes of transition-metal ions form a honeycomb lattice, similar to the one found in graphene. In this context, the discoveries that 2DEGs can also be created at the bare (001) surfaces of SrTiO₃ [14–16] and KTaO₃ [17, 18], and more recently at the (111) surface of KTaO₃ [19], opened new roads in the fabrication and study of different types of 2DEGs in TMOs –in particular using surface-sensitive spectroscopic techniques, which give direct information about the Fermi surface and subband structure of the confined states. The origin of the confinement is attributed to a local doping of the surface region due to oxygen vacancies and/or lattice distortions.

Here we show that new types of 2DEGs can be directly tailored at the bare (110) and (111) surfaces of SrTiO₃. Imaging their electronic structure *via* angle-resolved photoemission spectroscopy (ARPES), we find

that their Fermi surfaces, subband masses, and orbital ordering are different from the ones of the 2DEG at the SrTiO₃ (001) surface [14, 15] and the ones predicted for the bulk, being thus uniquely sensitive to the confining crystallographic direction. This occurs because the crystallographic symmetries of the 2DEG plane, and the electron effective masses along the confinement direction, influence the symmetry of the electronic structure and the orbital ordering of the t_{2g} orbitals. Furthermore, the observed carrier concentrations and 2DEG thicknesses for different surfaces allow us to showcase the impact of oxygen vacancies and of the polar discontinuity on distinctive features of the confined conducting sheet.

The confined states were either created by fracturing the samples in vacuum or by chemically and thermally preparing the surfaces *in situ*, and studied through ARPES at the Synchrotron Radiation Center (SRC, University of Wisconsin, Madison) and the Synchrotron Soleil (France). The sample preparation, similar to the one in references [20, 21], is detailed in the Supplemental Material [22]. All through this paper, we describe the crystal structure in a cubic basis of unit-cell vectors, and note as $[hkl]$ the crystallographic directions in real space, $\langle hkl \rangle$ the corresponding directions in reciprocal space, and as (hkl) the planes orthogonal to those directions.

The major difference between the confined states at various surface orientations of SrTiO₃ originates from the different symmetries of the corresponding crystal planes: 4-fold for the (001) plane, 2-fold for the (110) surface, and 6-fold for the (111) surface. Another difference is the polar character of the surface. Thus, while the (001) termi-

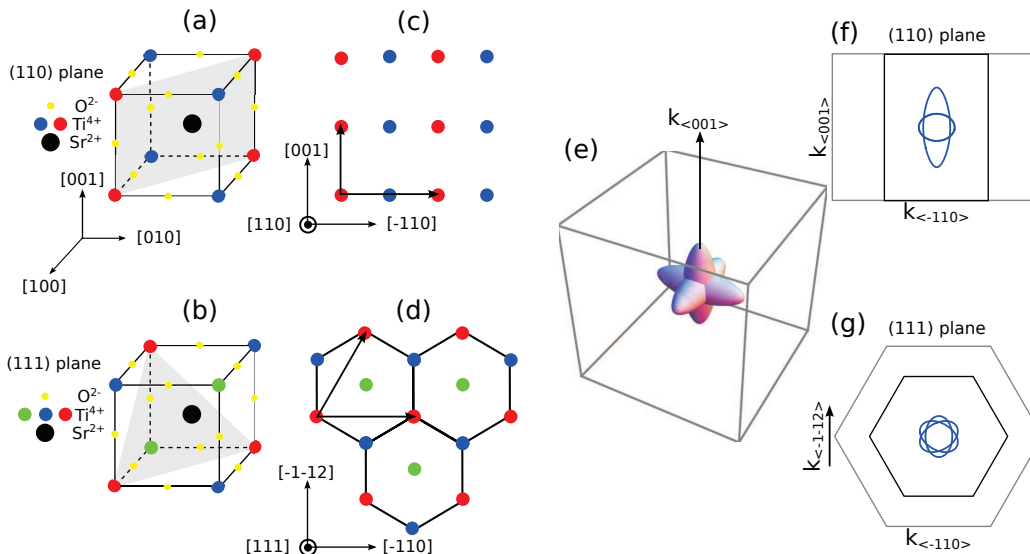


FIG. 1. (a, b) Unit cell of the cubic perovskite lattice of SrTiO_3 . The grey planes are the (110) and (111) planes, respectively. The yellow dots represent the O^{2-} anions, the black dot in the center the Sr^{2+} cation, and the red/green/blue dots the Ti^{4+} cations in different (110) or (111) planes. Both orientations are highly polar, as the crystal is built of alternating layers of $(\text{SrTiO})^{4+}$ and $(\text{O}_2)^{4-}$ or Ti^{4+} and $(\text{SrO}_3)^{4-}$. (c, d) Ti^{4+} cations of the crystal lattice at the (110) and (111) planes. The black arrows indicate the lattice vectors of the Ti^{4+} cations in one (110) or (111) plane. As indicated by the black lines in panel (d), a (111)-bilayer of Ti^{4+} cations forms a honeycomb lattice. (e) Bulk Fermi surface, calculated using a tight-binding model with an unrealistically large value of 10^{21} cm^{-3} for the bulk carrier density, intended to make the Fermi surface visible. Such carrier density is at least *three orders of magnitude* higher than the bulk carrier density of the samples prepared for this study. (f, g) Cross section of the bulk Fermi surface in (e) along the (110) and (111) planes, respectively. The grey lines show the cross section of the bulk 3D Brillouin zone through a Γ point, while the black lines correspond to the surface Brillouin zone.

nations, namely SrO or TiO_2 , are nominally non-polar, the (110) terminations are alternatively $(\text{SrTiO})^{4+}$ and $(\text{O}_2)^{4-}$, and the (111) terminations are either Ti^{4+} or $(\text{SrO}_3)^{4-}$. These different surface symmetries and their polarity are illustrated in figures 1(a-d). Note in particular, from figure 1(d), that a (111)-type bilayer of Ti^{4+} cations forms a honeycomb lattice, as noted in Ref. [10].

For our discussion later, it will be instructive to con-

TABLE I. Effective light (L) and heavy (H) masses predicted by a TB model in the bulk (first row) and experimental in-plane masses of the 2DEGs at the (001), (110), and (111) surfaces (other rows) along the different high-symmetry directions of the crystal lattice (columns) of SrTiO_3 . In the bulk, all the effective masses along (111) are identical.

	m_{100}/m_e		m_{110}/m_e		$m_{11\bar{2}}/m_e$		m_{111}/m_e
	L	H	L	H	L	H	
Theory bulk ^a	1.06	7.16	1.06	1.85	1.24	2.46	1.48
$\text{SrTiO}_3(001)$	0.7 ^b	10.0 ^b	0.7 ^c	1.3 ^c	0.8 ^c	1.8 ^c	1.0 ^c
$\text{SrTiO}_3(110)$	1.0	8.5	1.6	6.0	–	–	–
$\text{SrTiO}_3(111)$	–	–	0.27	1.08	0.33	8.67	–

^a From Ref. [23]

^b From Ref. [14]

^c From TB model using experimental masses along (100)

trast the observations at the (110) and (111) SrTiO_3 surfaces with both the 2DEG at the (001) surface and a model bulk electronic structure. Figure 1(e) shows the bulk Fermi surface from a simplified tight-binding (TB) model where the electron hopping amplitudes between the three t_{2g} orbitals of neighboring Ti^{4+} are $t_\pi = 0.236 \text{ eV}$ and $t_{\delta'} = 0.035 \text{ eV}$ [23], and we neglect spin-orbit coupling and tetragonal distortions. Near the Γ point, this gives effective masses listed in the first row of table I for various directions. Figures 1(f, g) show cross sections of the bulk Fermi surface along the (110) and (111) planes through the Γ point, illustrating their respective 2-fold and 6-fold symmetries. The *experimental* spectra at the SrTiO_3 (001) surface [14], on the other hand, fit well to a TB form where the hopping amplitudes are $\bar{t}_\pi = 0.36 \text{ eV}$ and $\bar{t}_{\delta'} = 0.025 \text{ eV}$, leading to values of the effective masses near the Γ point shown in the second rows of table I. Note that all these masses differ by about 30% from the bulk theoretical ones.

We now present our experimental results. Figure 2(a) shows the Fermi surface measured at the *fractured* (110) surface of an undoped *insulating* SrTiO_3 sample. As we will see, our observations are similar to another recent study of the 2DEG at the $\text{SrTiO}_3(110)$ surface in a Nb-doped sample prepared *in situ* by Wang *et al.* [24]. The metallic states we observe present the same 2-fold symmetry of the unreconstructed (110) surface Brillouin

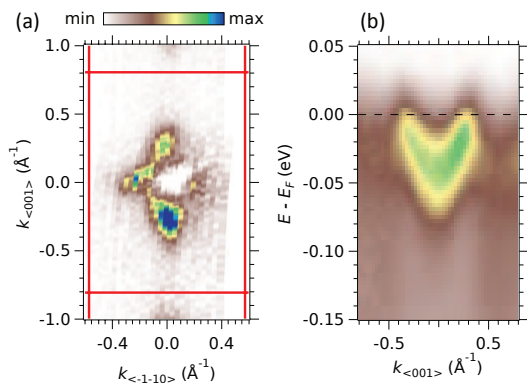


FIG. 2. (a) ARPES Fermi surface map (second derivative) at $h\nu = 91$ eV in the (110) plane of a fractured insulating SrTiO_3 sample. The map is a superposition of intensities measured in the bulk Γ_{130} and Γ_{131} Brillouin zones [22]. The red lines indicate the edges of the unreconstructed (110) Brillouin zones. (b) Energy-momentum intensity map at a Γ point along the $k_{(001)}$ direction.

zone (BZ), represented by red rectangles. This implies that (i) the macroscopic properties of this 2DEG should be highly anisotropic, echoing the observed anisotropic transport characteristics reported in 2DEGs at (110) $\text{LaAlO}_3/\text{SrTiO}_3$ interfaces [8], and (ii) any surface roughness or reconstructions, expected in this highly polar surface, do not affect the 2DEG, which must then reside in the sub-surface layers –in agreement with our previous conclusions on fractured (111) surfaces of KTaO_3 [19]. Figure 2(b) shows the dispersion along the $k_{(001)}$ direction, giving rise to the longest of the two ellipsoidal Fermi surfaces in figure 2(a). The band forming the shortest ellipsoid is eclipsed by photoemission selection rules along this direction (see the Supplemental Material [22]). The band bottom and Fermi momenta are about -40 meV and 0.3 \AA^{-1} , respectively.

From the data above, we model the Fermi surface of the 2DEG at the SrTiO_3 (110) surface as two orthogonal ellipses, one along along $\langle 001 \rangle$ with semi-axes of 0.3 \AA^{-1} and 0.1 \AA^{-1} , the other along $\langle 1\bar{1}0 \rangle$ with semi-axes 0.25 \AA^{-1} and 0.13 \AA^{-1} . From the area A_F enclosed by the Fermi surfaces, we obtain a carrier density $n_{2D}^{(110)} = A_F/2\pi^2 \approx 1 \times 10^{14} \text{ cm}^{-2}$. The electronic states associated to such a high charge carrier density *must be confined to the region near the surface* –otherwise the bulk would be highly conductive, in contradiction with the insulating nature of the samples studied. Similarly, from the band bottom and Fermi momenta, using a parabolic approximation, we obtain the effective band masses along $\langle 001 \rangle$ and $\langle 1\bar{1}0 \rangle$ (and equivalent directions), listed in the third row of table I. These effective masses are similar to the ones determined in the aforementioned study [24] of the 2DEG at the $\text{SrTiO}_3(110)$ surface. In our study, the band bottom of the heavy band, *c.f.* figure 2(b), and the carrier density of the 2DEG are slightly

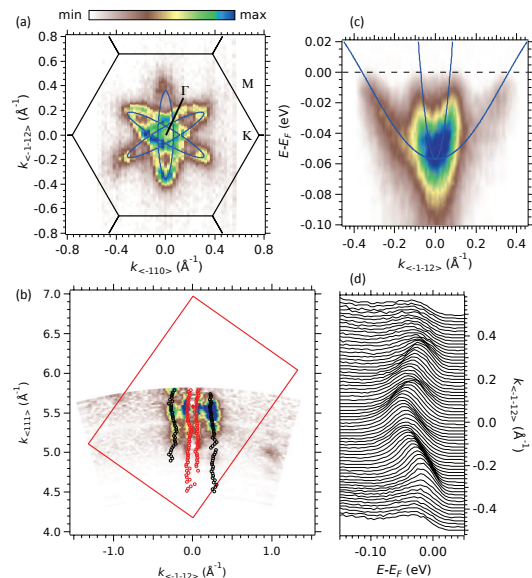


FIG. 3. (a) Fermi surface map measured at $h\nu = 110$ eV on a SrTiO_3 (111) surface prepared *in-situ*. The black lines indicate the edges of the unreconstructed (111) Brillouin zones around Γ_{222} . (b) Fermi surface map (second derivative of ARPES intensity, negative values) in the $k_{(111)} - k_{\langle 1\bar{1}2 \rangle}$, or $\langle 1\bar{1}0 \rangle$ plane, acquired by measuring at normal emission while varying the photon energy in 1 eV steps between $h\nu_1 = 67$ eV and $h\nu_2 = 120$ eV. The experimental Fermi momenta, represented by the black and red circles, were obtained by fitting the momentum distribution curves (MDCs) integrated over $E_F \pm 5$ meV. The red rectangle is the bulk Brillouin zone in the $\langle 1\bar{1}0 \rangle$ plane. (c) Energy-momentum map across the Γ point along the $\langle 1\bar{1}2 \rangle$ direction. The dispersions of a heavy band and light bands are visible. (d) Raw energy distribution curves of the dispersions shown in panel (c). In panels (a) and (c), the blue lines are simultaneous TB fits to the Fermi surface and dispersions.

lower, probably due to the different surface preparation techniques.

Henceforth, we focus on new experimental results at the (111) surface of SrTiO_3 , which as we will see presents the hexagonal symmetry of the unreconstructed surface, and could thus be an interesting platform for the quest of new electronic states and macroscopic properties at oxide surfaces.

Figure 3(a) shows the Fermi surface measured at the SrTiO_3 (111) surface prepared *in-situ*, as described in the Supplemental Material [22]. It consists of three ellipses forming a six-pointed star, thus strongly differing from the Fermi surface at the SrTiO_3 (110) surface, shown in figure 2(a), or the one at the SrTiO_3 (001) surface, discussed in previous works [14–16]. Additional experiments show that for surfaces prepared *in-situ* with either (1×1) or (3×3) reconstructions, the band structure and periodicity of the confined states are *identical*, and correspond to the one expected from an *unreconstructed surface* [22]. This indicates that the 2DEG at the $\text{SrTiO}_3(111)$ surface is also located in the sub-surface layers, and is at best weakly affected by the surface reconstructions at the po-

lar (111) surface.

The 2D-like character of the electronic states is strictly demonstrated from the Fermi surface map in the $\langle 111 \rangle - \langle \bar{1}\bar{1}2 \rangle$ plane, shown in figure 3(b). Here, one sees that the bands do not disperse along $k_{(111)}$ over more than half a bulk Brillouin zone, thereby confirming the confined (*i.e.*, localized) character of the electrons along the [111] direction in real space. The modulation of the intensity in the Fermi surface map, a typical feature of quantum well states [25, 26], is discussed in the Supplemental Material [22]. Interestingly, note that the red rectangles in figures 2(a) and 3(b) represent the Brillouin zone in the (110) (or equivalent) plane. Yet, as seen from those figures, the shapes of the corresponding Fermi surfaces are completely different. This directly shows the orientational tuning of the Fermi surface due to different confinement directions.

Figure 3(c) shows the energy-momentum map at the Γ point along the $\langle \bar{1}\bar{1}2 \rangle$ direction, corresponding to the major axis of the ellipsoids forming the 6-pointed-star Fermi surface. The dispersions of one light band and one heavy band are clearly visible. These constitute the ground state of the 2DEG. Additional subbands are not observed, implying that the band bending at the surface is too low to populate the upper quantum-well states. Within our resolution, the heavy and light bands are degenerate at Γ , with their band bottom located at about -57 meV. We fit simultaneously these dispersions and the whole Fermi surface of figure 3(a) using a simple tight-binding model [22]. The fit, shown by the continuous blue lines, yields Fermi momenta of about 0.07 \AA^{-1} and 0.36 \AA^{-1} for, respectively, the light and heavy bands along $\langle \bar{1}\bar{1}2 \rangle$. This gives an electron concentration $n_{2D}^{(111)} \approx 1.0 \times 10^{14} \text{ cm}^{-2}$, and effective masses listed in the third row of table I.

We now draw some comparisons between the effective masses and thicknesses of the 2DEGs at the SrTiO₃ (001), (110) and (111) surfaces. Table I shows that, while the masses along the “natural” electron-hopping directions in the bulk ([001] and equivalent) are comparable between the 2DEGs at the SrTiO₃ (001) and (110) surfaces, the masses along [110] at the (110) surface, and all the masses of the 2DEG at the (111) surface, are very different from the ones expected from the tight-binding parameters describing the bulk or the 2DEG at the (001) surface. In this respect, note that if the confinement direction is [110] or [111], then the electrons moving in the 2DEG plane along a direction *other than* [001] will experience the confining potential gradient and the modified crystal field outside the surface, as they will hop in staircase patterns between first neighbors along [001] (or equivalent) directions –see figures 1(a-d) and Ref. [8, 19]. The understanding of these mass differences, also reported in quantum well states at thin films of simple-metals [27] or strongly-correlated oxides [28], should be the subject of further theoretical works.

The maximal spatial extension d_{max} of the 2DEGs at the SrTiO₃ (110) and (111) surfaces can be estimated using a triangular potential well model [22]. We obtain $d_{max}^{110} \approx 1.7$ nm, which amounts to 6 2D-layers or 3 bulk unit cells along [110], and $d_{max}^{111} \approx 1.9$ nm, corresponding to ~ 9 layers of Ti (111), or again about 3 bulk unit cells along [111].

Finally, we note that the orbital ordering of the electronic states at the (110) and (111) surfaces of SrTiO₃ is different from the one at the (100) surface. In the first two cases, the bands are degenerate within our experimental resolution, whereas at the (001) surface the smallest observed splitting between bands of different orbital character is of 50 meV [14]. As the confinement energy of each band is inversely proportional to its effective mass along the confinement direction [14], different surface orientations result in different orbital ordering. But along the [111] direction the effective masses of the three t_{2g} bands are identical, and so their degeneracy at the Γ point is not lifted by the confinement. Similarly, the effective masses of bands of different orbital character along [110] are quite similar (see table I). Hence, the degeneracy lift is rather small, and cannot be observed in our data. This demonstrates the influence of the confinement direction on the orbital ordering.

Several scenarios have been proposed to explain the origin of the 2DEG at the LaAlO₃/SrTiO₃ (001) interface. According to one of these, the formation of a conducting sheet prevents the occurrence of a polar catastrophe in the material. Yet, the discovery of a confined 2DEG at the (001) surface of SrTiO₃, with characteristics similar to those of the above heterostructure, suggests that the driving mechanism may not be unique, as in the bare SrTiO₃ all the layers are electrically neutral. Instead, in the latter case, surface oxygen vacancies are believed to cause and to confine the gas [14, 15, 24]. Additionally, for the (110) and (111) SrTiO₃ surfaces, of nominal polar charge $4e$, one would expect a much larger carrier concentration in the 2DEG, and a very strong electric field confining the electrons in a narrow sheet at the surface. However, we observe that the carrier concentrations and thicknesses of the 2DEGs are quite comparable for all three orientations (this work and Ref. [14]): $n_{2D} \sim 10^{14} \text{ cm}^{-2}$, $d_{max} \sim 2$ nm. In fact, in the polar SrTiO₃ surfaces studied here, the polar catastrophe does not seem to be compensated by the electrons of the 2DEG but by surface reconstructions or relaxations, while the 2DEG lies in the subsurface layers. Thus, although the 2D electronic structure (effective masses, orbital ordering) depends on the surface orientation, the thickness and carrier concentration of the 2DEG might be controlled by another factor, probably oxygen vacancies and/or lattice distortions induced by the synchrotron light irradiation, as discussed in the Supplemental Material [22].

In conclusion, our results show that the symmetries, electronic structure, and orbital ordering of the con-

finned states at the surface of TMOs can be tailored by confining the electrons along different directions in the *same* material. Such orientational tuning echoes the differences of transport properties reported recently in $\text{LaAlO}_3/\text{SrTiO}_3$ (110) and (111) interfaces [7–9]. In particular, from our data, the highly anisotropic transport behavior observed in the (110) interfaces [8] can be directly related to the 2-fold symmetry of the Fermi surface measured by ARPES. More generally, our results provide an exciting route for obtaining new types of 2D electronic states in correlated-electron oxides.

We thank V. Pillard for her contribution to the sample preparation. T.C.R. acknowledges funding from the RTRA Triangle de la Physique (project PEGASOS). A.F.S.-S. and M.G. acknowledge support from the Institut Universitaire de France. This work is supported by public grants from the French National Research Agency (ANR) (project LACUNES No ANR-13-BS04-0006-01) and the “Laboratoire d’Excellence Physique Atomes Lumière Matière” (LabEx PALM project ELECTROX) overseen by the ANR as part of the “Investissements d’Avenir” program (reference: ANR-10-LABX-0039).

SUPPLEMENTAL MATERIAL

ARPES Experiments

The ARPES measurements were conducted at the Synchrotron Radiation Center (SRC, University of Wisconsin, Madison) and the Synchrotron Soleil (France). We used linearly polarized photons in the energy range 20 – 120 eV, and Scienta R4000 electron detectors with vertical slits. The angle and energy resolutions were 0.25° and 25 meV at SRC, and 0.25° and 15 meV at Soleil. The mean diameter of the incident photon beam was smaller than 100 μm . The samples were cooled down to 10-30 K before fracturing or measuring, in pressure lower than 6×10^{-11} Torr. The confined states were either created by fracturing the samples in vacuum or by chemically and thermally preparing the surfaces *in situ*, as detailed in the next section. The results were reproduced for at least five different samples for each surface orientation.

Surface preparation

The non-doped, polished crystals of SrTiO_3 were supplied by CrysTec GmbH and Aldrich. To prepare the surface, the samples were ultrasonically agitated in deionized water, subsequently etched in buffered HF and annealed at 950°C for several hours in oxygen flow. Depending on the annealing time, this treatment yields a Ti-rich, single-terminated or mixed-terminated step-and-terrace structured surface of SrTiO_3 (111) [20]. Fig-

ure 4(a) shows the atomic-force microscopy (AFM) image of the single-terminated (111) surface of a sample annealed for 3h. This treatment produces a (1×1) unreconstructed surface, shown by RHEED image in figure 4(b). Longer annealing (10h) results in a mixed-terminated surface [21], as shown in the AFM friction image in figure 4(c), measured in contact mode. The surface prepared in such a way is (3×3) reconstructed, as displayed in the RHEED image in figure 4(d). The surface state of the cleaved samples was not determined by imaging or diffraction techniques.

To perform the surface-sensitive ARPES measurements, one needs pristine and crystalline surfaces. To clean the surface of contaminations, the samples prepared as described above were further annealed *in-situ* in vacuum at a pressure of approximately $p = 3 \times 10^{-9}$ mbar at a temperature of $T = 550^\circ\text{C}$ for about 2 hours. This annealing step cleans the surface, does not change the surface reconstruction, and also introduces oxygen vacancies in the bulk of the SrTiO_3 samples. Note that the introduced bulk charge carrier density is at least three orders of magnitude lower than the one observed for the confined states in the ARPES measurements, as detailed in the main text. Moreover, Plumb *et al.* demonstrated that various *in-situ* sample preparations, including annealing in an O_2 -rich atmosphere which results in a non-doped bulk, create identical confined states at the (001) surface of TiO_2 -terminated SrTiO_3 [16]. Recall also, from figure 3(b), that the states observed in our experiments do not disperse along the confinement direction, which demonstrates their quasi-2D character.

For the confined states at the (111) surface, the quality of the obtained ARPES data is better for the surface prepared *in-situ*. This might be due to the strong polar nature of the (111) surface of SrTiO_3 . Hence, fracturing a sample along a (111) plane might yield a partly disordered surface.

The electronic structure of the 2DEG at the SrTiO_3 (111) surface is similar for the cleaved and the two differently prepared surfaces (unreconstructed and (3×3) reconstructed). In fact, for all three types of surfaces the periodicity of the electronic structure in reciprocal space, shown in figure 5(a) for the prepared, (3×3) reconstructed surface, corresponds to the one expected of an unreconstructed surface. By Bloch theorem, the very existence of dispersive bands and well-defined Fermi surfaces implies the existence of a periodic in-plane potential acting on the confined electrons, hence of crystalline order at the layer(s) where the 2DEG is located. As the electronic structure has the periodicity of the *unreconstructed* surface, the 2DEG seems to stabilize in a sub-surface region, where it is not affected by any surface reconstructions or superstructures related to vicinal surfaces or terraces. A possible explanation for this observation would be that the electrons of the Ti cations in the topmost layer are localized, while the itinerant elec-

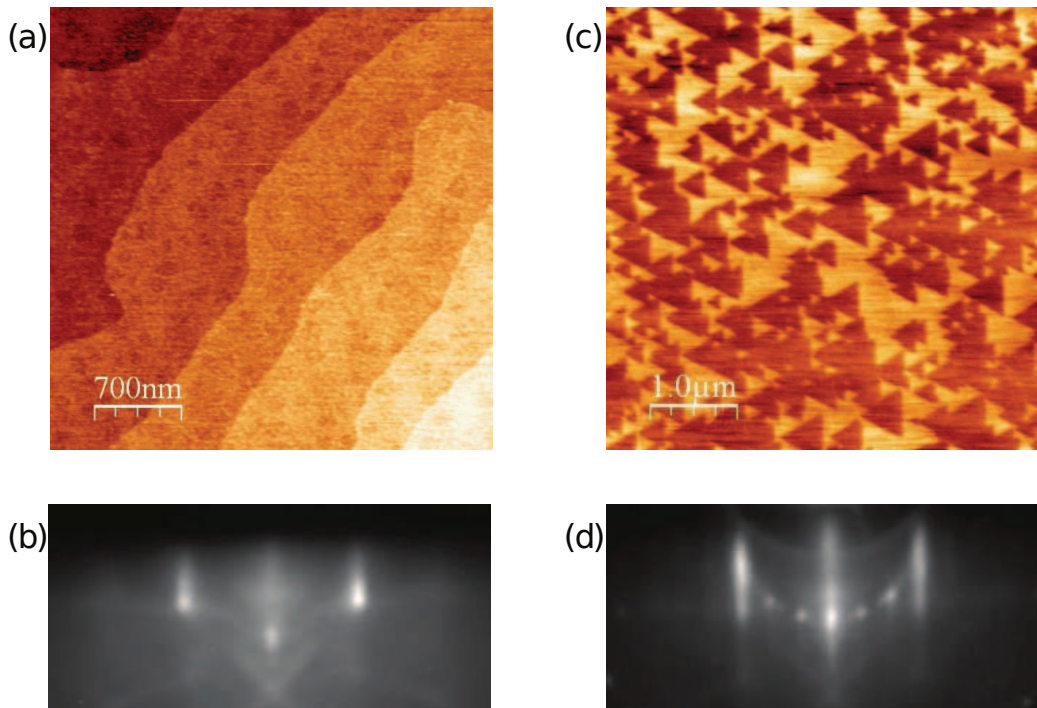


FIG. 4. (Color online) (a) Atomic force microscope (AFM) image of a chemically and thermally prepared SrTiO_3 (111) surface. The surface is single terminated and unreconstructed, as shown in the RHEED image in (b). Longer annealing times result in a mixed terminated surface, as demonstrated in the AFM friction image (c) measured in contact mode. A 3×3 reconstruction of the surface can be deduced from the corresponding RHEED image in (d).

trons exist in the subsurface layers. For the (110) surface, a surface preparation similar to the one described above for the (111) surface was conducted. The data quality of fractured and prepared samples are quite similar as the chemical etching step is not perfectly adapted to the (110) surface. Sr and Ti are both situated in one of the alternating (110) layers of $(\text{SrTiO})^{4+}$ and O_2^{4-} building up the crystal lattice. Thus, the selective etching of Sr-related species might result in a rather rough surface.

Photon energy dependence

The photon energy dependence of the electronic states at the SrTiO_3 (111) surface is displayed in the main text in figure 3. Although the states do not disperse, confirming their confined nature, the intensity of the states drops rather quickly moving away from Γ_{222} . This observation is similar to the intensity modulation as a function of the photon energy reported previously at the (001) surface of SrTiO_3 [14] and KTaO_3 [18], as well as in quantum well states of metals [25, 26]. This modulation is due to photoemission dipole selection rules: the optical excitation of the electrons occurs from initial states in the near surface region that do not disperse along the confinement direction (the confined electrons) to dispersing

bulk final states. Moreover, if the wave function of the confined states is not exactly localized in a 2D layer, but exists over several unit cells, the dispersion along the confinement direction will be affected. This can be intuitively understood from Heisenberg uncertainty principle: only a strict 2D confinement in real space yields a complete indetermination of the electron momentum along the confinement direction, hence an exactly cylindrical Fermi surface. Some delocalization along the confinement direction, as in quantum-well states, implies a small dispersion of the Fermi surface along that direction.

Bearing these effects (selection rules in quantum wells, finite delocalization) in mind, one can comprehend the data in figure 5(a), which shows a superposition of Fermi surface maps measured at different photon energies, for a (111) surface prepared *in-situ*. The black hexagons are the Brillouin zones assuming an unreconstructed surface. Thus, due to selection rules, the intensity of the photoemission peak from the confined states is highest close to positions corresponding to Γ points of the bulk, where final states at the same $k_{(111)}$ momentum are available for the optical transition. But this intensity will decrease rapidly by moving along $k_{(111)}$, away from the bulk Γ points [25]. Experimentally, this is done by changing the photon energy. This results in the necessity to measure in-plane Fermi surface maps at different photon energies,

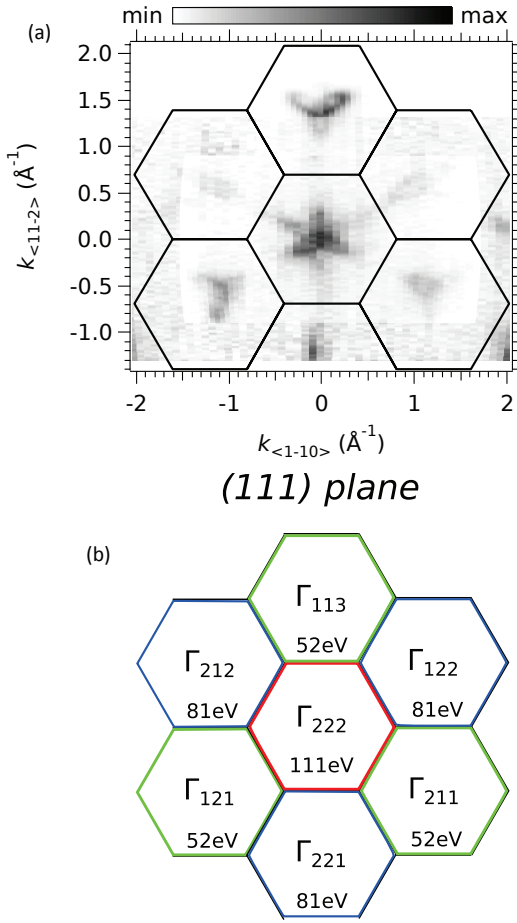


FIG. 5. (Color online) (a) Superposition of Fermi surface maps measured for the chemically and thermally prepared SrTiO₃ (111) sample (3×3) reconstructed surface) at photon energies of $h\nu = 47$ eV and $h\nu = 96$ eV. (b) Reciprocal 2D space in the (111) plane. Inside each Brillouin zone the projections of the different bulk Γ points corresponding to available final states during the photoemission process at the specified photon energy are indicated. This diagram helps understanding the Fermi-surface intensities shown in panel (a). The color (red, blue, green) of the hexagons indicates which Γ points are located in the same (111) plane in reciprocal space.

and then superpose them to retrieve the complete periodicity of the electronic states, as illustrated in figure 5(b). This figure shows the positions of the experimentally observed Γ points projected in the (111) plane. The photon energy inside each Brillouin zone corresponds to the k_{\perp} value of the Γ points assuming a work function of $W = 4.25$ eV and an inner potential of $V_0 = 12$ eV.

Fermi surface of SrTiO₃(110)

As stated in the main text, the Fermi surface map shown in figure 2 is a superposition of intensities measured in the bulk Γ_{130} and Γ_{131} Brillouin zones. Figure 6

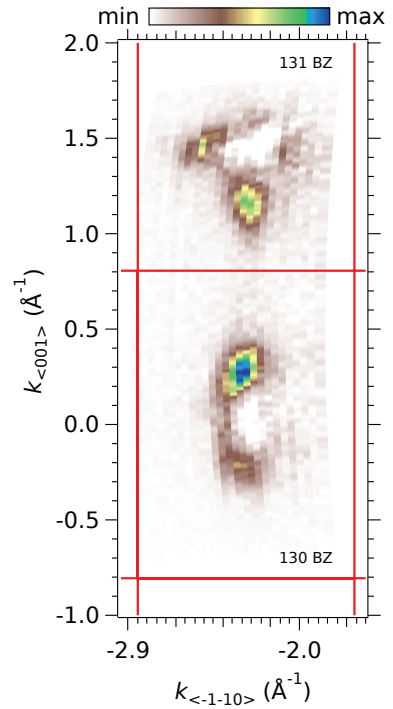


FIG. 6. (Color online) Second derivative of ARPES Fermi surface map at $h\nu = 91$ eV in the (110) plane of a cleaved insulating SrTiO₃ sample. The map spans the Γ_{130} (bottom) and Γ_{131} (top) Brillouin zones. The red lines indicate the edges of the unreconstructed (110) Brillouin zones.

shows the intensities measured in those Brillouin zones. Due to photoemission matrix elements, only the vertical ellipsoidal Fermi surface is observed around the Γ_{130} point, while both the vertical and the smaller horizontal ellipsoidal Fermi surfaces are observed around the Γ_{131} point.

Estimate of the spatial extensions of the 2DEGs at the SrTiO₃ (110) and (111) surfaces.

In our data, figures 2 and 3 of the main text, only the lowest-energy subbands are observed. To estimate the maximal extension d_{max} of the corresponding confined states, we follow the same strategy of Ref. [19]. We assume that the second subbands are slightly above the Fermi level, hence unoccupied and not detectable by ARPES. We then use a triangular potential well model, and take as effective masses along the [110] and [111] confinement directions, respectively, $m_{110} \approx 1.6m_e$ (the lightest of the masses gives the largest 2DEG thickness) and $m_{111} = 1.0m_e$ (given by extrapolating the experimental masses at the (001) surface to the bulk [111] direction) –see table I of the main text. This gives $d_{max}^{110} \approx 1.7$ nm, amounting to 6 2D-layers or 3 bulk unit cells along [110], and $d_{max}^{111} \approx 1.9$ nm, corresponding to

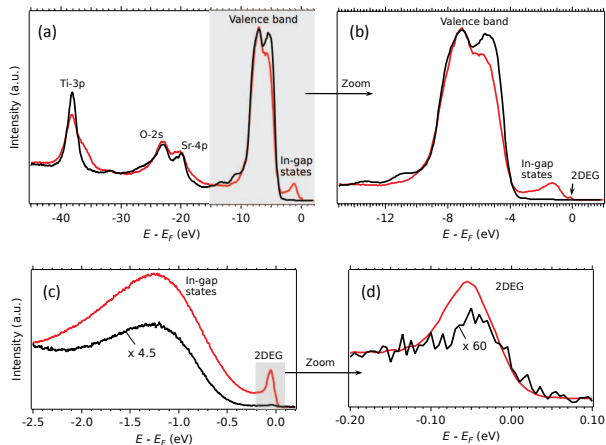


FIG. 7. (Color online) (a) Angle-integrated spectra of an SrTiO₃ sample prepared *in-situ*, measured at a photon energy of $h\nu = 110$ eV, with a step size of 50 meV, showing the density of states for binding energies between -45 eV and 2 eV. The black curve was measured shortly after the first exposure of the sample to the UV light, and the red curve at the end of the measurements (about 36 hours later). (b) Zoom over the valence band region. (c) Angle-integrated spectra showing the in-gap states and the confined states at the Fermi level, measured at $h\nu = 110$ eV with a step size of 5 meV. (d) Zoom over the confined states at the Fermi level.

~ 9 layers of Ti (111), or again about 3 bulk unit cells along [111].

UV dose dependence: enhancement of Ti³⁺ signal

Understanding the influence of the UV synchrotron illumination on the observed confined states is important to determine the origin of such states. Recent photoemission studies on the 2DEGs at the (001) or (110) surface of SrTiO₃ proposed that the UV light creates oxygen vacancies [15, 24] or, respectively, ferroelectric lattice distortions [16] in the surface region. The two effects are difficult to disentangle using photoemission, as in both cases charge is transferred from O to Ti. Figure 7(a) shows the angle-integrated spectra, measured at $h\nu = 110$ eV, of a SrTiO₃ sample prepared *in-situ* for binding energies between -45 eV and 2 eV. The black curve was measured shortly after the first exposure of the sample to the UV light, while the red curve was recorded at the end of the measurements (36 hours later). The spectra are normalized to the intensity of the Sr 4*p*-peak, which should be rather independent of the concentration of oxygen vacancies and/or ferroelectric lattice distortions. Figure 7(b) is a zoom over the valence band region, while figures 7(c, d) show the in-gap states and the confined states at the Fermi level. The change of various features under UV irradiation is obvious: first, the formation of a shoulder in the Ti-3*p* peak at lower binding energies, indicating electron transfer from Ti⁴⁺ to a lower valency state. Second,

the decrease in intensity of the valence band in its low binding energy region. Third, the increase in intensity of the in-gap states and of the peak corresponding to the confined states. All these observations could be explained by both scenarios: the creation of oxygen vacancies and the ferroelectric lattice distortions.

In contrast to samples prepared *in-situ*, cleaved samples show a different behavior regarding the UV light exposure. The subbands of the 2DEG in all the *cleaved* SrTiO₃ surfaces we have studied so far, *i.e.* (001), (110) and (111), are all observed essentially *immediately after cleaving*, with no or little time delay after the first exposure to UV light. A more detailed study on the UV induced effects is beyond the scope of this paper.

Tight-binding calculations of the 2DEG at the SrTiO₃(111) surface

The band dispersions shown in the main text correspond to the bottom of the conduction band of SrTiO₃, which is formed by Ti-3*d* orbitals hybridized with O-2*p* orbitals. The interaction between the oxygen anions forming an octahedron and the Sr cation generates a large crystal field which splits the *d* states in a lower *t*_{2*g*} triplet and an higher *e*_g doublet. Hence, only the *t*_{2*g*} orbitals are considered in our tight-binding model, which is based on the calculations of reference [10]. Our model for the SrTiO₃(111) surface is limited to a bilayer of Ti atoms. This approach is sufficient to fit the experimental data as shown in the main text, but does not necessarily imply the confinement of the electrons to a bilayer.

The Hamiltonian H of the system in the basis $\{d_{I,n}\}$, where $I = (X, Y, Z)$ correspond to the orbital character (*yz*, *zx*, *xy*) of the *t*_{2*g*} orbitals and $n = 1, 2$ indicates the number of the layer of Ti cations, is given by:

$$H = \begin{pmatrix} d_{X,1}^\dagger \\ d_{Y,1}^\dagger \\ d_{Z,1}^\dagger \\ d_{X,2}^\dagger \\ d_{Y,2}^\dagger \\ d_{Z,2}^\dagger \end{pmatrix}^T \begin{pmatrix} \tilde{\epsilon}_X & & \epsilon_X & & & \\ & \tilde{\epsilon}_Y & & \epsilon_Y & & \\ & & \tilde{\epsilon}_Z & & \epsilon_Z & \\ \epsilon_X^* & & & \tilde{\epsilon}_X & & \\ & \epsilon_Y^* & & & \tilde{\epsilon}_Y & \\ & & \epsilon_Z^* & & & \tilde{\epsilon}_Z \end{pmatrix} \begin{pmatrix} d_{X,1} \\ d_{Y,1} \\ d_{Z,1} \\ d_{X,2} \\ d_{Y,2} \\ d_{Z,2} \end{pmatrix}$$

Here, $\tilde{\epsilon}_I$ describes the hopping of electrons between next nearest neighbors of Ti cations (intra-layer hopping), characterized by the hopping amplitude $t_{\sigma''}$, whereas ϵ_I describes the hopping between nearest neighbors (inter-layer hopping) with hopping amplitudes t_π and t'_δ :

$$\begin{aligned}
\tilde{\epsilon}_X &= -2t_{\sigma''} \cos\left(-\frac{\sqrt{3}}{2}\tilde{a} k_x + \frac{3}{2}b k_y\right) \\
\tilde{\epsilon}_Y &= -2t_{\sigma''} \cos\left(\frac{\sqrt{3}}{2}\tilde{a} k_x + \frac{3}{2}b k_y\right) \\
\tilde{\epsilon}_Z &= -2t_{\sigma''} \cos(\sqrt{3}\tilde{a} k_x) \\
\epsilon_X &= -t_{\pi} e^{-i\tilde{a} k_y} \left[1 + e^{i\frac{\tilde{a}}{2}(-\sqrt{3}k_x+3k_y)}\right] - t_{\delta'} e^{i\frac{\tilde{a}}{2}(\sqrt{3}k_x+k_y)} \\
\epsilon_Y &= -t_{\pi} e^{-i\tilde{a} k_y} \left[1 + e^{i\frac{\tilde{a}}{2}(\sqrt{3}k_x+3k_y)}\right] - t_{\delta'} e^{i\frac{\tilde{a}}{2}(-\sqrt{3}k_x+k_y)} \\
\epsilon_Z &= -2t_{\pi} e^{i\frac{\tilde{a}}{2} k_y} \cos\left(\frac{\sqrt{3}}{2}\tilde{a} k_x\right) - t_{\delta'} e^{-i\tilde{a} k_y}.
\end{aligned}$$

In the above expressions, k_x corresponds to $k_{\langle 1\bar{1}0 \rangle}$, k_y to $k_{\langle 1\bar{1}2 \rangle}$, and \tilde{a} to the cubic lattice constant a projected in the (111) plane $\tilde{a} = \sqrt{2/3}a$. Compared to the calculations of reference [10], our data can be fitted rather well using a simplified model. We neglect in our model the spin-orbit coupling, the trigonal crystal field, the layer potential difference, crystal distortions at low temperature, and the hopping ($t_{\pi'}$) between next nearest neighbors of different orbital symmetry. The fits shown in figures 3(a) and 3(c) of the main text are based on such a simplified model using fitting parameters of $t_{\pi} = 1.6$ eV, $t_{\delta'} = 0.07$ eV and $t_{\sigma''} = 0.05$ eV.

Note that such value of t_{π} , which quantifies the hopping energy between nearest neighbors along the [100] (and equivalent) directions, is here over 4 times larger than the same parameter inferred from the 2DEG at the SrTiO₃ (001) surface (namely, $t = 0.36$ eV, see the main text). This shows again that the effective masses of the 2DEG at the SrTiO₃ (111) surface strongly differ from what would be expected from a model based on the 2DEG at the (001) surface. As discussed in the main text, the electrons moving along any direction in the (111) plane will actually hop in zig-zag patterns between first neighbors along [001] (or equivalent) directions, and thus will experience the confining potential gradient and the modified crystal field outside the surface. These effects are not accounted by our minimalist TB model. Additionally, our TB model only considers one bilayer of Ti atoms. However, it is known that in quantum well states the effective masses of the confined electrons depend on the width of the quantum well or, equivalently, the number of layers [27, 28]. All these effects should be taken into account in future theoretical works addressing the 2DEGs at the different surfaces of SrTiO₃. On the other hand, while distortions of the crystal lattice, and thereby of the overlap between the different t_{2g} orbitals, might exist at the surface and be slightly different depending on the surface orientations, they should bear a negligible effect on the 2DEGs reported here, as we have seen that their electronic structure is essentially insensitive to surface polarity or reconstructions.

* andres.santander@csnsm.in2p3.fr

- [1] H. Takagi and H. Y. Hwang, An Emergent Change of Phase for Electronics, *Science* **327**, 1601 (2010).
- [2] J. Mannhart and D.G. Schlom, Oxide Interfaces—An Opportunity for Electronics, *Science* **327**, 1607 (2010).
- [3] S.Thiel, G. Hammerl, A. Schmehl, C. W. Schneider, J. Mannhart, Tunable Quasi-Two-Dimensional Electron Gases in Oxide Heterostructures, *Science* **313**, 1942 (2006).
- [4] A.D. Caviglia, S. Gariglio, N. Reyren, D. Jaccard, T. Schneider, M. Gabay, S. Thiel, G. Hammerl, J. Mannhart, J.-M. Triscone, Electric field control of the LaAlO₃/SrTiO₃ interface ground state, *Nature (London)* **456**, 624 (2008).
- [5] A. Brinkman, M. Huijben, M. van Zalk, J. Huijben, U. Zeitler, J.C. Maan, W.G. van der Wiel, G. Rijnders, D.H.A. Blank, H. Hilgenkamp, Magnetic effects at the interface between non-magnetic oxides, *Nat. Mater.* **6**, 493 (2007).
- [6] M. Salluzzo, S. Gariglio, X. Torrelles, Z. Ristic, R. Di Capua, J. Drnec, M. Moretti Sala, G. Ghiringhelli, R. Felici, N.B. Brookes, Structural and Electronic Reconstructions at the LaAlO₃/SrTiO₃ Interface, *Adv. Mater.* **25**, 2333 (2013).
- [7] G. Herranz, F. Sánchez, N. Dix, M. Scigaj, J. Fontcuberta, High mobility conduction at (110) and (111) LaAlO₃/SrTiO₃ interfaces, *Sci. Rep.* **2**, 758 (2012).
- [8] A. Annadi *et al.*, Anisotropic two-dimensional electron gas at the LaAlO₃/SrTiO₃ (110) interface, *Nat. Commun.* **4**, 1838 (2013).
- [9] G. Herranz, N. Bergeal, J. Lesueur, M. Scigaj, N. Dix, J. Fontcuberta, Orientational tuning of the 2D-superconductivity in LaAlO₃/SrTiO₃ interfaces, *arXiv:1305.2411* (2013).
- [10] D. Xiao, W. Zhu, Y. Ran, N. Nagaosa, S. Okamoto, Interface engineering of quantum Hall effects in digital transition metal oxide heterostructures, *Nat. Comm.* **2**, 596 (2011).
- [11] K.-Y. Yang, W. Zhu, D. Xiao, S. Okamoto, Z. Wang, Y. Ran, Possible interaction-driven topological phases in (111) bilayers of LaNiO₃, *Phys. Rev. B* **84**, 201104 (2011).
- [12] A. Rüegg and G.A. Fiete, Topological insulators from complex orbital order in transition-metal oxides heterostructures, *Phys. Rev. B* **84**, 201103 (2011).
- [13] D. Doennig, W.E. Pickett, R. Pentcheva, Massive Symmetry Breaking in LaAlO₃/SrTiO₃(111) Quantum Wells: A Three-Orbital Strongly Correlated Generalization of Graphene, *Phys. Rev. Lett.* **111**, 126804 (2013).
- [14] A.F. Santander-Syro *et al.*, Two-dimensional electron gas with universal subbands at the surface of SrTiO₃, *Nature (London)* **469**, 189 (2011).
- [15] W. Meevasana, P.D.C. King, R.H. He, S.-K. Mo, M. Hashimoto, A. Tamai, P. Songsiriritthigul, F. Baumberger, Z.-X. Shen, Creation and control of a two-dimensional electron liquid at the bare SrTiO₃ surface, *Nat. Mater.* **10**, 114 (2011).
- [16] N.C. Plumb *et al.*, Mixed dimensionality of confined conducting electrons tied to ferroelectric surface distortion on an oxide, *arXiv:1302.0708*, (2013).
- [17] P.D.C. King *et al.*, Subband Structure of a Two-

- Dimensional Electron Gas Formed at the Polar Surface of the Strong Spin-Orbit Perovskite KTaO_3 , *Phys. Rev. Lett.* **108**, 117602 (2012).
- [18] A.F. Santander-Syro *et al.*, Orbital symmetry reconstruction and strong mass renormalization in the two-dimensional electron gas at the surface of KTaO_3 , *Phys. Rev. B* **86**, 121107 (2012).
- [19] C. Bareille *et al.*, Two-dimensional electron gas with six-fold symmetry at the (111) surface of KTaO_3 , *Sci. Rep.* **4**, 3586 (2014).
- [20] A. Biswas, P.B. Rossen, C.-H. Yang, W. Siemons, M.-H. Jung, I.K. Yang, R. Ramesh, Y.H. Jeong, Universal Ti-rich termination of atomically flat SrTiO_3 (001), (110), and (111) surfaces, *Appl. Phys. Lett.* **98**, 051904 (2011).
- [21] J. Chang, Y.-S. Park, S.-K. Kim, Atomically flat single-terminated SrTiO_3 (111) surface, *Appl. Phys. Lett.* **92**, 152910 (2008).
- [22] See Supplemental Material [URL] for more details on the sample preparation, photon energy dependent matrix elements, the Fermi surface of $\text{SrTiO}_3(110)$, spatial extensions of the 2DEGs and the UV dose dependence of the photoemission spectra.
- [23] G. Khalsa and A.H. MacDonald, Theory of the SrTiO_3 surface state two-dimensional electron gas, *Phys. Rev. B* **86**, 125121 (2012).
- [24] Z. Wang, Z. Zhong, X. Hao, S. Gerhold, B. Stoger, M. Schmid, J. Sanchez-Barriga, A. Varykhalov, C. Franchini, K. Held, U. Diebold, Anisotropic two-dimensional electron gas at $\text{SrTiO}_3(110)$, *PNAS* **111**, 3933 (2014).
- [25] A. Mugarza, J. Ortega, A. Mascaraque, E. Michel, K. Altmann, F. Himpfel, Periodicity and thickness effects in the cross section of quantum well states, *Phys. Rev. B* **62**, 12672 (2000).
- [26] E.D. Hansen, T. Miller, T.C. Chiang, Quantum-well or bulklike behaviour of Cu layers on Co, *J. Phys.: Condens. Matter* **9**, L435 (1997).
- [27] Y.Z. Wu, C.Y. Won, E. Rotenberg, H.W. Zhao, F. Toyoma, N.V. Smith, Z.Q. Qiu, Dispersion of quantum well states in $\text{Cu/Co/Cu}(001)$, *Phys. Rev. B* **66**, 245418 (2002).
- [28] K. Yoshimatsu, K. Horiba, H. Kumigashira, T. Yoshida, A. Fujimori, M. Oshima, Metallic Quantum Well States in Artificial Structures of Strongly Correlated Oxide, *Science* **333**, 319 (2011).